

## Growth, Reaction and Nanowire Formation of Fe on the ZnS(100) Surface

Ka Lun Man<sup>1,†</sup>, Anastassia Pavlovska<sup>1,2</sup>, Ernst Bauer<sup>1,2</sup>, Andrea Locatelli<sup>3</sup>, Tevfik O. Menteş<sup>3</sup>, Miguel A. Niño<sup>3,‡</sup>, George K. L. Wong<sup>1</sup>, Iam Keong Sou<sup>1</sup> and Michael S. Altman<sup>1,\*</sup>

<sup>1</sup>Department of Physics, The Hong Kong University of Science and Technology, Kowloon, Hong Kong

<sup>2</sup>Department of Physics, Arizona State University, Tempe, AZ 85287, USA

<sup>3</sup>Elettra-Sincrotrone Trieste S.C.p.A., 34149 Basovizza, Trieste, Italy

\*E-mail: phaltman@ust.hk

### Abstract

The growth and reaction of Fe on a ZnS(100) substrate are studied in situ and with high lateral resolution using Low Energy Electron Microscopy (LEEM), micro Low Energy Electron Diffraction ( $\mu$ LEED), X-ray Photoemission Electron Microscopy (XPEEM), microprobe X-ray Photoelectron Spectroscopy ( $\mu$ XPS) and X-ray Magnetic Circular Dichroism PEEM (XMCDPEEM) for complementary structural, chemical and magnetic characterization. Initially, a two-dimensional (Fe, Zn)S reaction layer forms with thickness that depends on growth temperature. Further growth results in the formation of a variety of three-dimensional crystals, most of them strongly elongated in the form of “nanowires” of two distinct types, labeled as A and B. Type A nanowires are oriented near the ZnS [110] direction and are composed of Fe. Type B nanowires are oriented predominantly along directions a few degrees off the ZnS[001] direction and are identified as Greigite ( $\text{Fe}_3\text{S}_4$ ). Both types of nanowires are magnetic with Curie temperatures above 450°C. The understanding of the reactive growth mechanism in this system that is provided by these investigations may help to develop growth methods for other elemental and transition metal chalcogenide nanostructures on ZnS and possibly on other II-VI semiconductor surfaces.

---

<sup>†</sup> Present Address: Femtosecond Spectroscopy Unit, Okinawa Institute of Science and Technology, Graduate University, Okinawa, Japan 904-0495.

<sup>‡</sup> Present Address: IMDEA Nanociencia, Cantoblanco 28049 Madrid, Spain.

## 1. Introduction

The growth of Fe on semiconductor surfaces, in particular on GaAs, and the magnetic properties of the resulting films have been studied extensively during the past few decades, motivated mainly by the desire to use Fe as spin injector into the semiconductor for magneto-electronic (spintronic) devices [1]. This line of investigation has also been extended to the growth of Fe on wide band gap semiconductors. It was found that Fe grows on thin epitaxial (100)-oriented ZnS films on GaP(100) substrates at temperatures between 350°C and 400°C in the form of nanowires (NWs), using ex situ transmission electron microscopy and electron diffraction [2-4]. Recently, magnetic nanowires have been the subject of numerous studies because of their unique physical properties and promising applications in spin-related nanotechnologies such as high-density magnetic recording, magnetic field sensors, magnetic nanoprobes for spin-polarized microscopy and cell manipulation in biomedical technology [5-9]. In particular, ferromagnetic nanowires are ideal one-dimensional nanostructures for studying the motion, manipulation and logic operation of magnetic domain walls [10-12] as well as the predicted ballistic anisotropic magnetoresistance [13].

In order to understand the mechanisms that lead to NW growth on ZnS(100) [2-4], we have studied the same system in situ using the laterally resolving surface science technique low energy electron microscopy (LEEM) combined with micro low energy electron diffraction ( $\mu$ LEED) [14-15]. The real-time imaging capability of LEEM allows in situ monitoring of growth dynamics.  $\mu$ LEED can provide diffraction information from very small selected areas, which is indispensable for studying spatially inhomogeneous systems, as we observe here. In addition, X-ray Photoemission Electron Microscopy (XPEEM), microprobe X-ray Photoelectron Spectroscopy ( $\mu$ XPS) and X-ray Magnetic Circular Dichroism Photoemission Electron Microscopy (XMCDPEEM) [16-17] have been used in order to identify the chemical composition and magnetic state of the crystals grown on ZnS(100). Our

investigations of growth were carried out at temperatures in the range 260-400°C, which covers the range studied previously, but also extends it to lower temperatures. Furthermore, we employed Fe deposition rates here that were about ten times lower than used in previous investigations [2-4]. This difference from previous growth conditions was chosen in order to explore growth behavior closer to equilibrium.

The in-situ multi-technique approach used here provides clear evidence that Fe reacts with ZnS(100) at high temperatures producing a (Fe,Zn)S reaction layer but that the reaction layer formation is suppressed at lower growth temperature. This temperature-dependent reaction is shown to play a very important role in subsequent NW nucleation and growth behavior. The highly laterally resolved measurements performed here also identify the composition of type A NWs as pure Fe and type B as greigite ( $\text{Fe}_3\text{S}_4$ ). The discovery of factors that give rise to the growth of highly elongated type B NWs strengthens our understanding of the vapor-solid reaction that underpins its use as an alternative to numerous other approaches to greigite nanostructure formation in the laboratory, for example, by cultivation in magnetotactic bacteria [18], hydro- or solvo-thermal methods [19-21] and pyrolysis of single source precursors and other chemical methods [22-28]. The morphologies revealed in the present investigations consequently contribute to further proposed developments of magnetic greigite nanoparticle applications that include diverse biomedical [26, 27, 29] to energy storage and conversion functionalities [20, 25, 30].

## **2. Experimental**

### *2.1. ZnS sample preparation*

The ZnS(100) samples used in this study were fabricated in the same VG V80H MBE system as in previous studies [2-4]. The ZnS layers are grown on a GaP(100) substrate, which is used because of its small lattice mismatch (0.76%) and the same crystal structure as ZnS, therefore

allowing high quality ZnS epitaxial growth. Before the substrate is loaded into the MBE system, it was first degreased with tetrahydrofuran for 5 minutes. Then the tetrahydrofuran was removed by soaking the substrate in acetone and rinsing in high grade deionized water (with resistivity greater than 18MΩcm). Afterward, the substrate was etched in a solution of  $\text{NH}_4\text{OH} : \text{H}_2\text{O}_2 : \text{H}_2\text{O} = 1:1:10$  for 10 minutes and finally rinsed with high grade deionized water and dried with  $\text{N}_2$  gas. After the chemical cleaning treatment, the substrate was mounted on an indium free Mo block and loaded into the MBE system. The GaP substrate was deoxidized at 610°C, after which a 50nm ZnS layer was grown at 200°C using an effusion cell containing high purity ZnS. The surface structure was monitored with reflection high energy electron diffraction (RHEED) during growth, and the observation of a bright and streaky RHEED pattern indicated the growth of a high quality ZnS. After the growth of the ZnS layer, the sample was removed from the MBE system and stored in dry nitrogen to prevent oxidation and water condensation.

## *2.2. ZnS(100) in situ surface preparation and Fe deposition*

The growth of Fe on ZnS(001) surface was studied in situ using LEED and LEEM in the LEEM instrument at the Hong Kong University for Science and Technology (HKUST) and using XPS, XPEEM, XMCDPEEM, LEEM and LEED in the Spectroscopic Photo Emission and Low Energy Electron Microscopy (SPELEEM) instrument at the Synchrotron Radiation facility Elettra in Trieste, Italy. Before deposition of Fe, the ZnS samples were outgassed in UHV at around 340°C, until a sharp (1x1) diffraction pattern was observed in LEED. The intensity difference between the LEED spots in the  $[011]$  and  $[01\bar{1}]$  directions of the surface and the domain structure that was observed in the LEEM images indicated qualitatively a miscut towards the  $[01\bar{1}]$  direction. However, the miscut was not investigated carefully using LEED spot-profile analysis. Fe was deposited using electron beam heated evaporators, which

were equipped with water cooling and an internal flux monitor. The deposition rate was calibrated via the monolayer growth of Fe on W(110) and W(100) surfaces. The corresponding deposition rates, measured in units of the atomic density of the ZnS (100) surface, were 0.58 monolayers (ML)/min at HKUST and 0.37 ML/min at Elettra. A W-3%Rh/W-25%Rh thermocouple was used to measure sample temperature at HKUST. A W-5%Rh/W-26%Rh thermocouple and an infrared pyrometer were used to monitor the sample temperature at Elettra.

### **3. Results and discussion**

#### *3.1. Growth, morphology and structure of Fe on ZnS(100)*

The growth of Fe on ZnS(100) was studied at different temperatures in the range 260°C–400°C. Nineteen ZnS samples (12 at HKUST and 7 at Elettra) were used in the growth experiments. Each sample was used for a single growth experiment. The samples cannot be reused because it was not possible to remove reversibly the grown crystals from the ZnS epitaxial layer and to return to a pure intact ZnS layer. The amount of deposited Fe in the different experiments varied from 10 to 18 ML.

Two types of NWs, with crystal shapes similar to those described in the earlier studies [2-4] have been observed together with many other previously unreported crystal shapes. One type labeled as type A NWs in the previous study [2] have almost always their longer axis along the ZnS substrate [011] direction (figure 1(a)). Very seldom they grow along the  $[01\bar{1}]$  direction but are not elongated as they are when they grow along the [011] direction, which is attributed to the substrate miscut mentioned before. These NWs are generally irregular in shape, and their  $\mu$ LEED pattern (figure 2(a)-(b)) has a unit mesh with reciprocal lattice vectors corresponding well with those of the bcc-Fe (100) plane parallel to the substrate, with the Fe[001] parallel to the ZnS[011] direction. The spots frequently are streaked at oblique

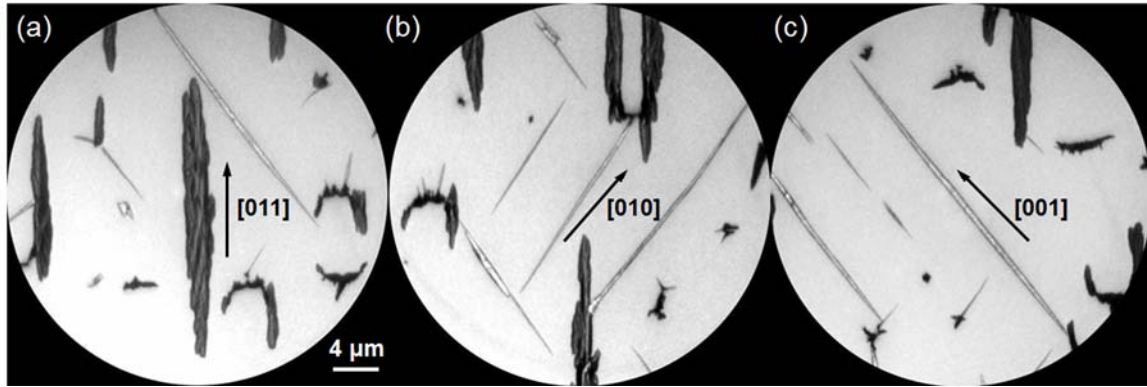


**Figure 1.** LEEM images of most common type A (a) and type B (b,c) nanowires oriented along the [011] direction (a), few degrees off [010] direction (b) and few degrees off [001] direction (c). LEEM image at 10 eV.

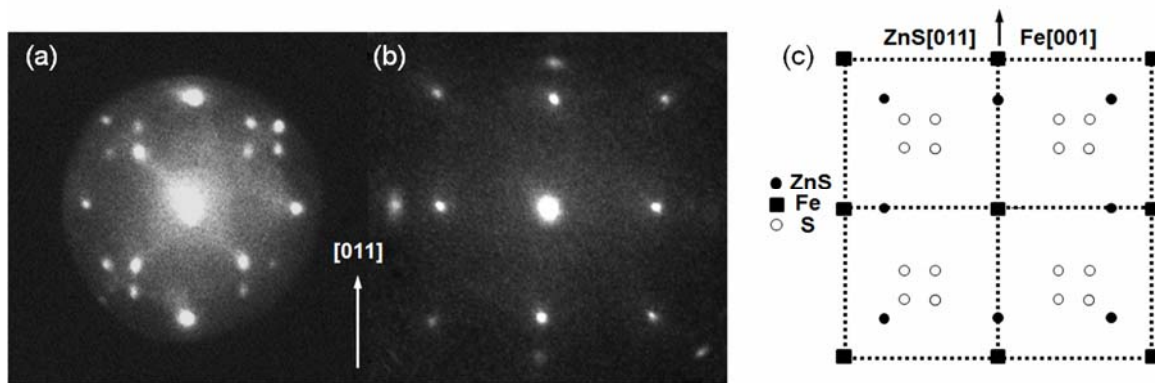


**Figure 2.**  $\mu$ LEED patterns of type A NWs at (a) 17 eV, (b) 42 eV. The ZnS [011] direction is shown in the figure. c) Schematic drawing of the LEED pattern with spots indicated from the ZnS substrate (ZnS), type A NWs (Fe) and S-induced NW surface reconstruction (S). The Fe [001] and ZnS [011] directions are parallel.

angles, indicating the presence of facets. Extra spots appearing in the LEED pattern at the center of the Fe unit cell can be attributed to the presence of  $c(2 \times 2)$  antiphase boundary domains typical for 0.5ML of chemisorbed sulfur on the Fe (100) surface [31-33]. Figure 2(c) shows a schematic drawing of the observed LEED pattern of type A NWs. The strong ZnS diffraction spots in the  $\mu$ LEED patterns shown in figure 2 are attributed to the fact that the 2  $\mu$ m diameter  $\mu$ LEED beam illuminates the ZnS as well as the NW.

The type B NWs, shown in figure 1(b) and figure 1(c), have regular shape, are generally thinner and have a much larger length to width ratio than the type A NWs. The type

B NWs grow with their long axis predominantly along directions a few degrees off the [001] and [010] directions of the ZnS substrate. Some of the NWs are oriented along the [018] and [081] substrate directions (7 degrees from [001] and [010] directions) in agreement with the earlier study [2]. However, it is not uncommon to find type B NWs, oriented along other directions near [011],  $[01\bar{1}]$ ,  $[0\bar{1}8]$  and  $[08\bar{1}]$  directions. NWs that grow in the directions along and near to [001] and [010] (figures 1(b) and 1(c)) are usually the narrowest and have sharp pointed tips, giving needle-like appearance. On the contrary, the type B NWs that grow in the [011] direction or near to it are wider, short and have blunted ends.

Despite their many different orientations, all type B NWs can be clearly distinguished from type A and other nanostructures by the identical set of superstructure spots in their diffraction patterns. This set of spots is shown in figure 3 for a NW aligned along the [018] direction (a few degrees off the ZnS substrate [001] direction). In a LEEM instrument, the spot positions in the LEED pattern do not depend on electron energy for surfaces parallel to the substrate, and thus any movement of diffraction spots identifies the presence of surfaces tilted to the substrate. In the case of type B NWs, some superstructure spots do not move

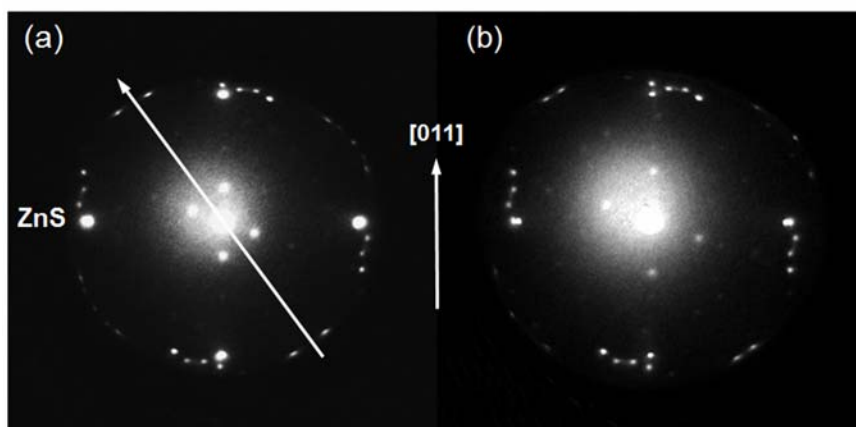


**Figure 3.**  $\mu$ LEED pattern of a type B NW oriented (long arrow in (a)) a few degrees off the ZnS [001] direction at (a) 17 eV, (b) 20 eV. The four brightest outer spots in (a) are from the ZnS substrate. The quadruplets of spots next to the ZnS spots, belong to the type B NW. The four inner spots and outer spots that move with increasing energy indicate the presence of facets on the NW. The ZnS [011] direction is shown.

when the incident electron beam energy is changed (outer spots in figures 3(a) and 3(b)). Other diffraction spots move across the diffraction pattern when the incident electron energy varies (inner spots in figures 3(a) and 3(b)). These spots are caused by facets on the NW surfaces. Information about the facet plane in type B NWs is extracted by mapping out the position of the facet spots in reciprocal space following established procedures [34-37]. From the reciprocal space map, we determined that facets are present on the sides of the NWs that are tilted roughly  $30^\circ$  relative to the underlying ZnS(100) surface and the (100) plane on top of the NW.

The lattice parameters of the unit meshes and the facet planes of the type B NWs do not fit to the crystal structure of either bcc- or fcc-Fe. This leads to the conclusion that type B NWs are rather a reaction product of Fe with the substrate instead of pure Fe. The Fe-S system, in particular, has many different phases and its phase diagram is rather complex [38, 39]. The only compound listed in the published Fe-S phase diagrams that can produce the observed diffraction pattern is greigite ( $\text{Fe}_3\text{S}_4$ ). A quantitative analysis of the diffraction pattern, which is presented in a separate paper [40], combined with the observation reported below that the type B NWs are magnetic with a high Curie temperature (see Sect. 2.5), confirms this conclusion. The crystals have (100) orientation with a (100) top plane and  $\{522\}$  facets on both sides. Details can be found in reference 40.

The growth morphology of Fe NWs on ZnS(100) was observed to depend very strongly on temperature in the temperature range studied (260-400°C). The goal of our study was to understand the conditions for the growth of the type B NWs with very long and thin needle-like shape. Figure 4 shows the morphology observed after growth of Fe on ZnS(100) at different growth temperatures using different growth procedures. The fields of view of these images are the same so that differences in the density of the crystals and in their shape and size can be seen.

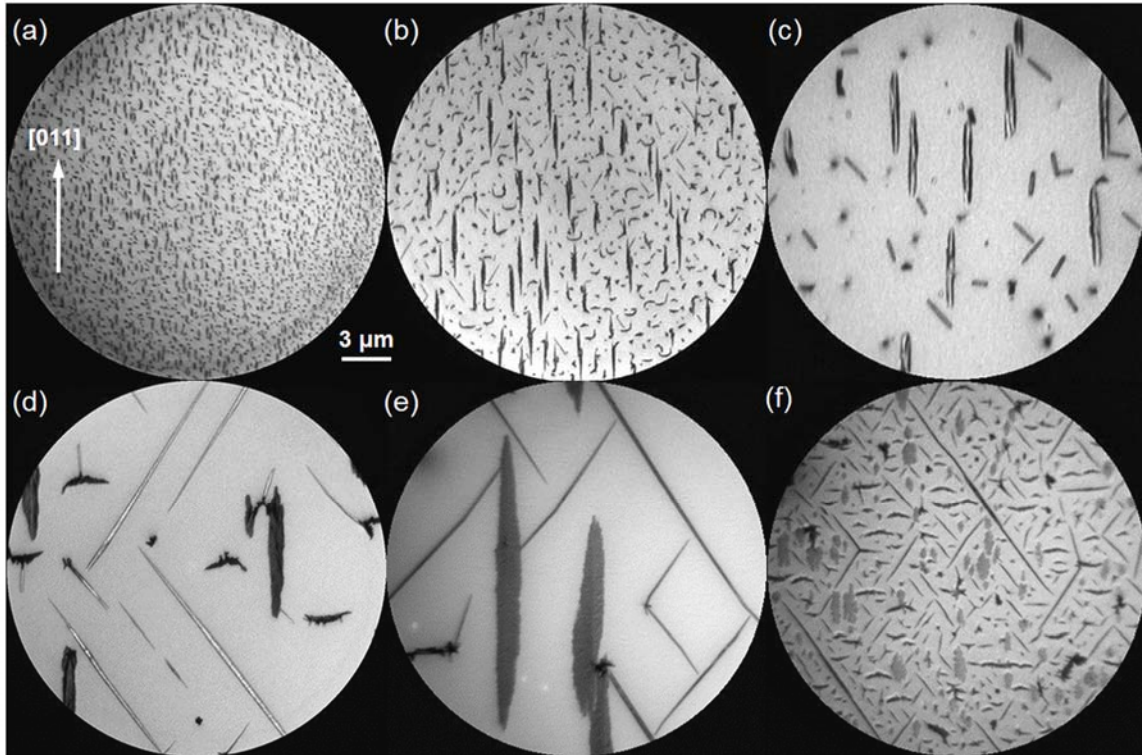


**Figure 4.** NWs morphology at different growth conditions: (a) deposition of 11.5 ML Fe at 325°C followed by cooling to 300°C, LEEM image at 10 eV, (b) deposition at 365°C until nucleation, second deposition after cooling to 300°C totaling 7.3 ML, LEEM image at 10 eV, (c) deposition of 16.4 ML at 357°C, LEEM image at 5 eV, (d) deposition of 3.5 ML at 360°C followed by deposition of 11.5 ML during cooling to 270°C, LEEM image at 10 eV, (e) deposition of 3ML at 368°C followed by deposition of 11.5 ML during cooling to 275°C, LEEM image at 3 eV, (f) the deposition at 372°C was interrupted after 2 ML before the nucleation occurs. The sample was left at this temperature for 40 min. Then the deposition was resumed during cooling from 372 to 260°C totaling 13 ML, LEEM image at 4.5 eV. The ZnS [011] direction is shown.

At lower temperatures (260°C and 280°C) a high density of very small crystals with size comparable or less than 10 nm was observed. At 325°C (figure 4(a)) the growing crystals are still small and their density is high. Figure 4(b) shows the morphology observed using a ‘two temperatures’ approach: first deposition at high temperature (365°C) until nucleation started and second deposition after cooling to lower temperature (300°C). The density of the crystals is still high, despite the low nucleation rate at 365°C because nuclei also form subsequently with high density during the second stage of growth at 300°C. The crystal density produced by growth entirely at temperature of about 360°C is noticeably much lower

(figure 4(c)) but the type B NWs are short and have flat ends, regardless of their orientation. The best results, from the point of view of growing needle-like type B NWs, were obtained using a variable temperature approach (figures 4(d)-(f)). Instead of interrupting the growth by stopping the deposition at high temperature before decreasing the temperature, it was continued during cooling. In the experiments shown in figure 4(d) and figure 4(e), only 3.5 and 3.0 ML, respectively, were deposited at high temperatures 360° and 368°C, respectively, followed by longer deposition during cooling to 270° and 275°C, respectively. This approach produced the desired needle-like type B NWs. In the experiment shown in figure 4(f), the variable temperature procedure was different: the deposition at 372°C was interrupted after 2ML were deposited before the nucleation occurs. The sample remained at the same high temperature for 40 min. The deposition was resumed after 40 min and nucleation occurred while cooling from 372° to 260°C. This approach resulted in elongated type B NWs mixed with a wide variety and high density of other crystals.

Figure 5 shows the NW growth sequence from real-time LEEM observations during the variable temperature approach that leads to the formation of needle-like type B NWs. Fe was deposited at 370°C until nucleation occurred. Thereafter, the temperature was decreased rapidly to 260°C during deposition. During this process, the temperature initially dropped by 83°C over the first two minutes and then it decreased somewhat slower. The sample temperatures in figures 5(a)-(c) are 320°C, 270°C and 260°C, respectively, and the final Fe coverage in (c) is 7.4 ML. When the temperature decreased during cooling, narrow type B NWs begin to grow out rapidly from seed nuclei that were formed initially at higher temperature. This procedure avoids the proliferation of nuclei that form during deposition at low temperature, seen for example in figures 4(a) and 4(b). The avoidance of nucleation at low temperature permits the growth of very long needle-like type B NWs whose low density is determined by the low nucleation rate at high temperature.

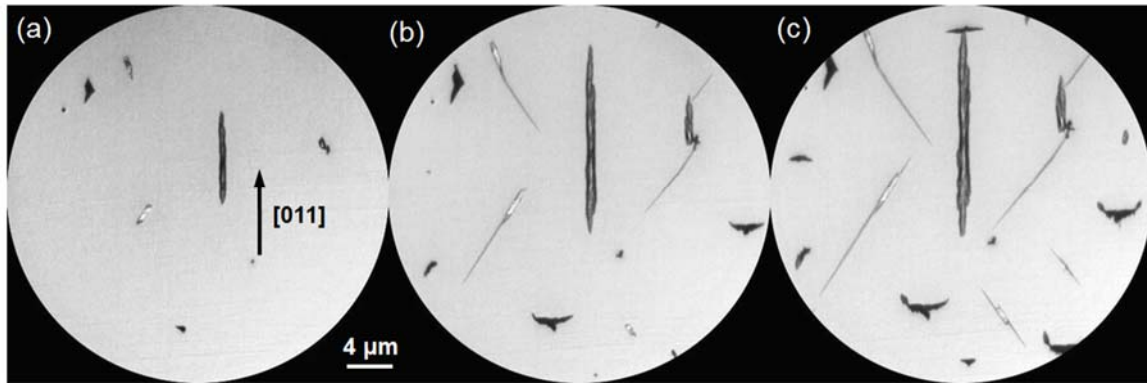


**Figure 5.** Growth of nanowires during the variable temperature approach. LEEM images at 10 eV. Initially, 2.6 ML Fe was deposited at 370°C. After nucleation, the temperature was decreased rapidly to 260°C during continuous deposition. Narrow nanowires grow at lower temperature. The Fe coverages and sample temperatures for images (a)-(c) are 3.4, 5.4 and 7.4 ML and 320°C, 270°C and 260°C, respectively. The ZnS [011] direction is shown.

To summarize, the type B NWs grown by using the variable temperature approach starting at high temperatures (360°-370°C) followed by cooling, have sharp tips, grow up to lengths of 30-50  $\mu\text{m}$  and are about 100 nm wide. Their length to width aspect ratio is typically 300:1 up to 500:1.

### 3.2. Growth mechanism, chemical composition and reaction layer

A key question that the observations presented in the previous section raise is the nature of the NW growth mechanism, particularly the underlying reasons for the dramatic temperature dependence of the type B NWs formation. This question can be addressed by real-time observations of growth with LEEM. From these observations, the bright field image intensity formed using the (0,0) beam at fixed incident electron energy was extracted as a function of time. Figure 6(a) shows the intensity/time dependence of two experiments at different temperatures. During the initial phase of the growth at high temperature, 363°C, the intensity increases with an inflection at 4.4 min, which corresponds to the deposition of 2.48 ML Fe at the observed onset of crystal nucleation. The intensity continues to increase slightly up to 5 min and remains constant (saturated) during further deposition. During growth at lower

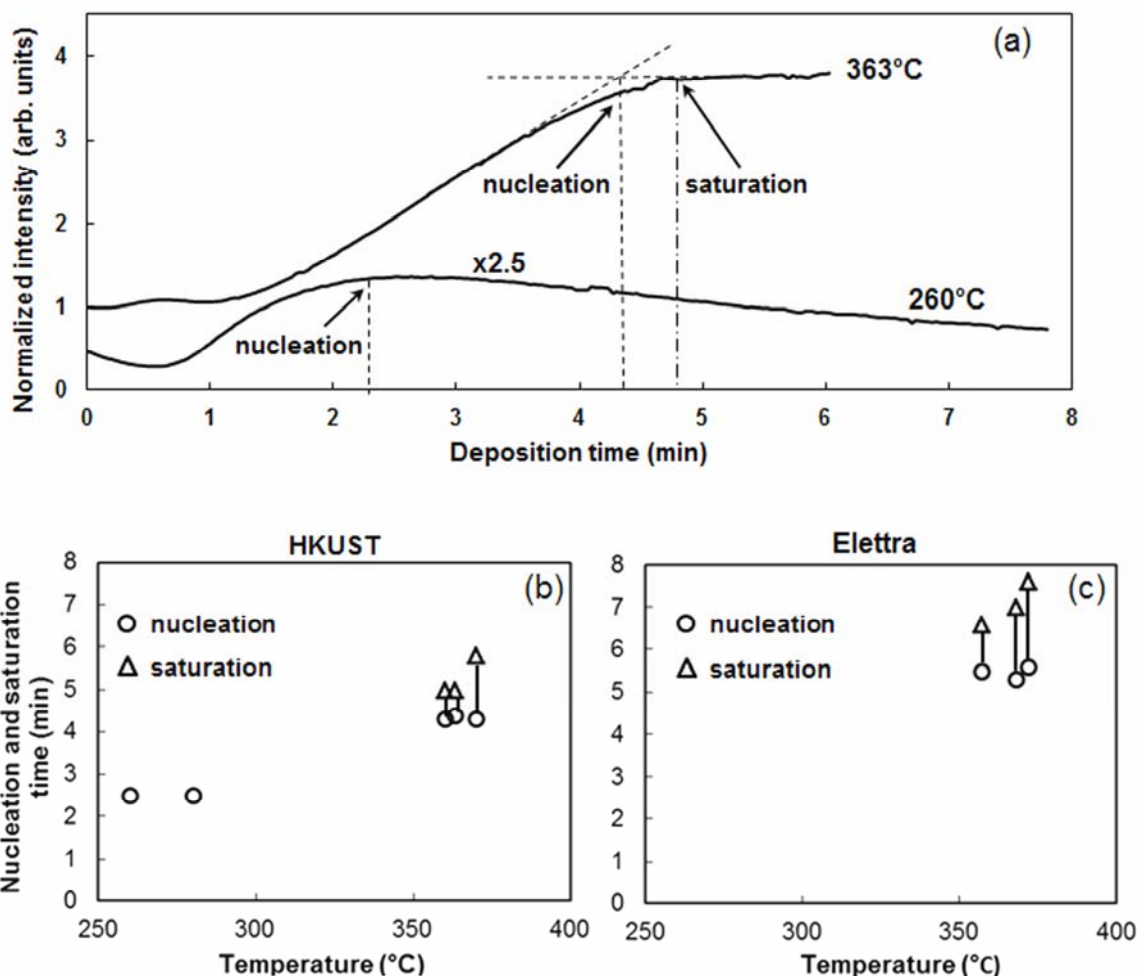


**Figure 6.** (a) LEEM image intensity as a function of time during Fe deposition at 363°C and at 260°C. LEEM imaging energy 10 eV. The lower curve is multiplied by 2.5 and shifted downward by 0.5 arb. units. (b,c) The temperature dependence of the time for nucleation and of the time for intensity saturation is shown for different experiments performed at (b) HKUST and (c) Elettra.

temperature, 260°C, the intensity increase is significantly smaller and the nucleation occurs earlier (at 2.5 min). The intensity has a maximum at nucleation and decreases during further deposition. At the nucleation onset, only 1.44 ML Fe were deposited compared with 2.48 ML at the high temperature (upper curve).

The intensity change during the initial layer growth and the crystal nucleation were both observed to depend strongly on temperature at given (constant) deposition rate. At lower temperatures (260-280°C) the intensity decreases after the maximum at the onset of nucleation and no intensity saturation was observed. At higher temperatures (360-370°C) the

intensity increased more strongly and a longer time was needed for the onset of nucleation. Another important difference is that at high temperatures, the intensity does not reach a maximum but continues to increase after the nucleation until it saturates. These trends are demonstrated further in figure 6(b), which shows the temperature dependence of the nucleation and saturation time for the experiments performed at HKUST. Figure 6(c) show the temperature dependence of the nucleation and saturation time for the experiments in Elettra, where only experiments at high temperatures were performed.

We attribute the unusually strong dependence of the nucleation rate on temperature and the results of the intensity measurements to reaction of Fe with the ZnS substrate. This view is supported by chemical characterization described below. At high temperature, this reaction readily produces a (Fe,Zn)S surface layer before nucleation occurs, while the reaction rate below about 360°C is low and crystals nucleate on a mostly unreacted substrate surface. At high temperatures, the deposited Fe (usually about 2 - 2.5 ML Fe) is initially consumed by the reaction producing a (Fe,Zn)S reaction layer. If we assume that every second Zn atom is replaced by Fe, then 4 ML of ZnS had to be modified by the reaction with 2 ML Fe prior to nucleation at high temperature. Reaction and nucleation/growth are competing processes. The gradual intensity saturation after nucleation suggests that nucleation does not immediately stop the reaction to form more (FeZn)S. The reaction continues after nucleation but at diminishing rate as the ZnS layer becomes more saturated with Fe and the growing Fe NWs more effectively accumulate deposited Fe. The intensity saturation indicates that the reaction progresses no further. At very high temperature, 395°C, the reaction rate is so high that nucleation and image intensity saturation were observed only after deposition of much more Fe.

The reaction of Fe with the ZnS substrate helps to explain also why the longest needle-like type B NWs grow when deposition is started at high temperature, 360-370°C and

continued without interruption during cooling. The nucleation rate following the formation of the reaction layer at high temperatures is very low (figures 4(d) and 4(e)), producing a small number of NWs at high temperature that act as sinks for the diffusing S and Fe atoms. This diminishes further nucleation during cooling and promotes the growth of longer NWs. Reduced nucleation on the reaction layer can also be seen by comparing nucleation on the unreacted surface during growth entirely at low temperature, e.g. at 325°C in figure 4(a), with nucleation at low temperature on the reacted surface, e.g. at 300°C (figure 4(b)), during the two temperature approach. The reaction layer itself that is formed at high temperature also appears to be essential for the growth of type B NWs, whose composition differs from the pure Fe type A NWs as confirmed by the chemical characterization described below. Another factor that likely contributes to the formation of highly elongated type B NWs during the variable temperature approach is the effect of cooling on kinetic processes.

The chemical compositions of the NWs and the ZnS substrate under Fe flux were determined by core level  $\mu$ XPS measurements in the SPELEEM at the Nanospectroscopy beamline at Elettra. The spectra were obtained from a stack of images taken at fixed photon energy as a function of kinetic energy of the photoelectrons in steps of 0.1 eV for Zn and S and 0.2 eV for Fe over the energy ranges shown in figures 7 and 8; computer controlled data acquisition enabled us to appropriately adjust the image focus as a function of the photoelectron kinetic energy, following a calibration made prior to the experiments. The local XPS spectra were obtained by setting integration windows on selected regions of interest in the image stack. The surface of type A NWs consists mainly of (100) surfaces parallel to the substrate, while the central region of narrower type B NWs is also a (100) plane bounded by inclined {522} facets [40]. Although the spherical aberration of the objective lens can lead to a slight overlap of the emission from outside the selected region of interest, the emission from the type B nanowire facets is partially filtered out by the contrast aperture. For these reasons

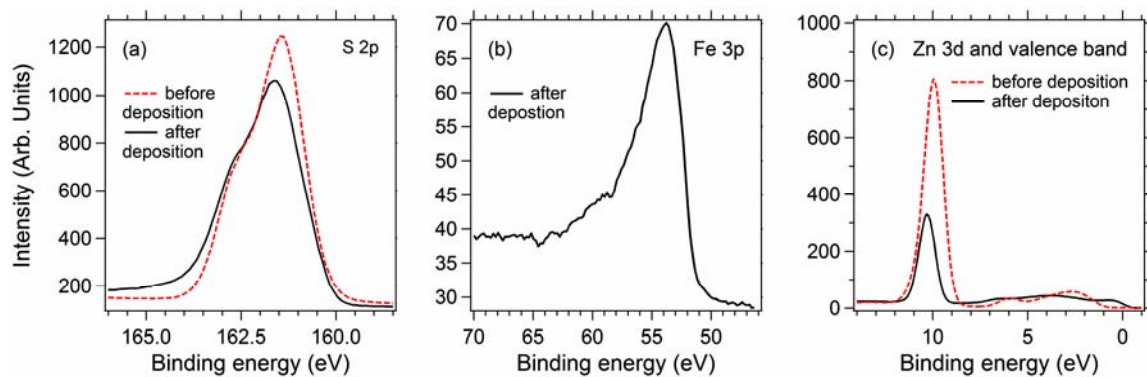


**Figure 7.**  $\mu$ XPS spectra of the ZnS substrate taken before Fe deposition and after depositing 1.9 ML Fe at 370°C before nucleation started. S 2p emission decreased by about 6.5% and Zn 3d emission decreased by about 32% after the deposition.

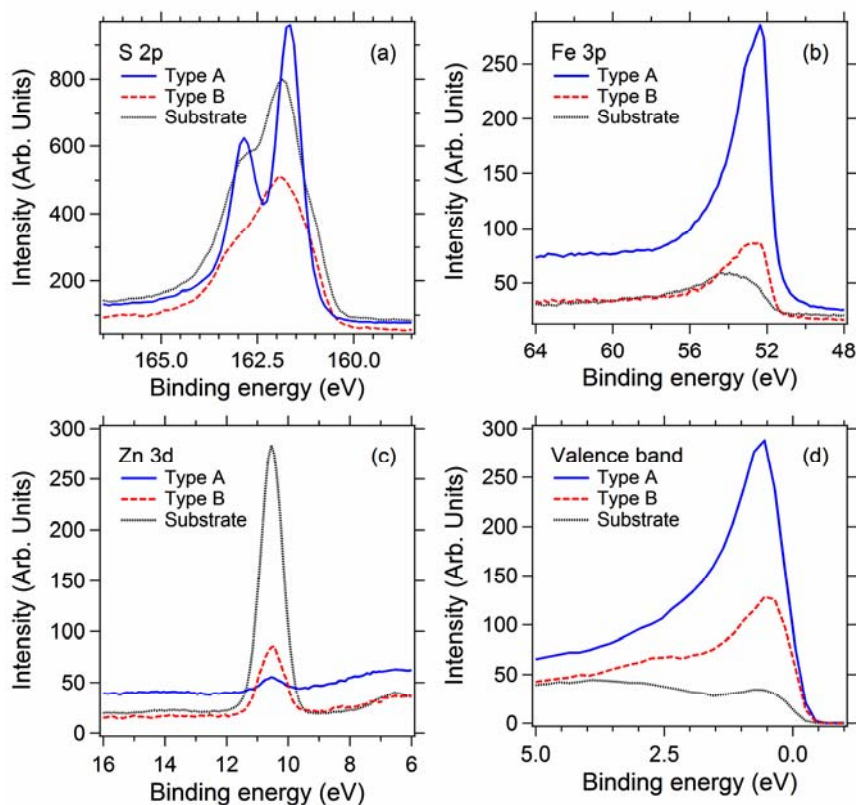


**Figure 8.**  $\mu$ XPS taken from selected regions after deposition of 14.6 ML Fe at 368°C-275°C. (a) (S 2p) spectra show comparable amount of S on the nanowires and on the substrate; (b) (Fe 3p) spectra show less Fe on type B than on type A nanowires and a significant amount of Fe on the substrate surface; (c) (Zn 3d) spectra show very little zinc on nanowires; (d) The valence band spectra show Fermi edge for both types nanowires and for the substrate.

a quantitative analysis of the spectra cannot be made. In the following we discuss the results of the detailed analysis of the spectra shown in figures 7 and 8. The detailed spectra analysis

is presented together with the detailed analysis of the LEED patterns elsewhere [40]. In the spectra presented in figures 7 and 8, binding energies were referenced to the Fermi level (when possible) or to 1s core level emission of graphitic C (at 284.0 eV in our system).

In order to understand the reaction of Fe with the ZnS substrate (the reaction layer), XPS spectra were taken before Fe deposition and after depositing only 1.9 ML Fe at 370°C before nucleation started. Figure 7 shows that the S 2p signal has decreased 6.5% and shifted nearly 0.2 eV to higher binding energy due to Fe deposition. The decrease is unexpected because the surface still shows a sharp LEED pattern with the same lattice constant as before reaction, indicating good surface order, though with somewhat stronger background, probably caused by defects. The signal decrease may be caused by a stronger attenuation of the S 2p photoelectrons in the surface layer in which Zn has been replaced by Fe. The Zn liberated in the reaction is desorbed because the vapor pressure is in the range of  $10^{-3}$  Torr to  $10^{-1}$  Torr in the temperature range of the experiments. This replacement is clearly indicated by the strong decrease of the Zn 3d signal to about 32% of its original value. In addition, the Zn peak is shifted by about 0.4 eV to higher binding energy due to Fe deposition. These changes are attributed to the replacement of the Zn atoms in about 4 ML of the ZnS layer, assuming the composition  $\text{Fe}_{0.5}\text{Zn}_{0.5}\text{S}$ . It is also possible that Fe is distributed over more layers with lower concentration per ML. The slight increase of the lattice constant that should occur with increasing Fe concentration from 5.409 Å in ZnS to 5.424 Å in  $\text{Fe}_{0.5}\text{Zn}_{0.5}\text{S}$  [41] is within the limits of error of the  $\mu\text{LEED}$  measurement. The energy shifts are a natural result of the change of the chemical environment of the respective atoms. The reaction also causes the band gap to disappear, making the surface metallic.

Figure 8 shows  $\mu\text{XPS}$  taken from type A NWs, from type B NWs and from the substrate surface in between after variable temperature deposition of 14.6 ML Fe at 368°C to 275°C. In the sulfur (S 2p) spectra (figure 8(a)), a comparable amount of S is seen on the

NWs and on the substrate. Standard fitting procedures of the spectra show that the type A NW spectrum can be fitted with one 2p doublet, typical for adsorbed layers, while the type B NW and substrate spectra require two doublets for fitting, typical for Fe sulfides [40]. The sulfur spectra for type A and B NWs in figure 8(a) are affected by several factors, including the inelastic mean free path of photoelectrons and the different angular distributions of emitted electrons, which affects the instrument transmission. Due to these factors a quantitative analysis of the sulfur spectra in our study is difficult. The iron (Fe 3p) spectra (figure 8(b)) show much less Fe on type B than on type A NWs and also a significant amount of Fe on the substrate surface. The small magnitude of the zinc (Zn 3d) signal (figure 8(c)) is not a reliable measure for the relative amount of Zn in the three regions because of the limitations of  $\mu$ XPS in the SPELEEM, which could cause some cross talk between very narrow features such as the type B wires and the surrounding surface. Probably, there is little if any Zn on the type A and B NWs. For the Fe and S signals of type A and B crystals, cross talk is a minor problem because their Fe and S (adsorbed on A and incorporated in B) signals are very high so that a small cross talk changes the signal only slightly within the limits of error. This issue is discussed at greater length in reference 40. The valence band spectra (figure 8(d)) show a clear Fermi edge for the type A and B NWs, thus metallic behavior. When the substrate spectrum is enhanced to the same peak height as that of the type A NWs, its edge coincides with that of the type A NW spectrum, therefore the surface layer sampled by the photoelectrons is also metallic.

### *3.3. Magnetic characterization*

The magnetic characterization has been performed by XMCDPEEM in the SPELEEM instrument at the Nanospectroscopy beamline in Elettra. In XMCDPEEM, the x-ray energy is tuned to the Fe  $L_3$  edge at 707eV and two PEEM images at opposite x-ray helicity are

subtracted to obtain the maps of the in-plane component (parallel to the x-ray beam) of the magnetic domains [16, 17]. Both type-A and type-B NWs produce a magnetic signal in the XMCDPEEM images at room temperature (figure 9) showing that they are both ferromagnetic or ferrimagnetic. Type A NWs prepared by deposition at constant temperature

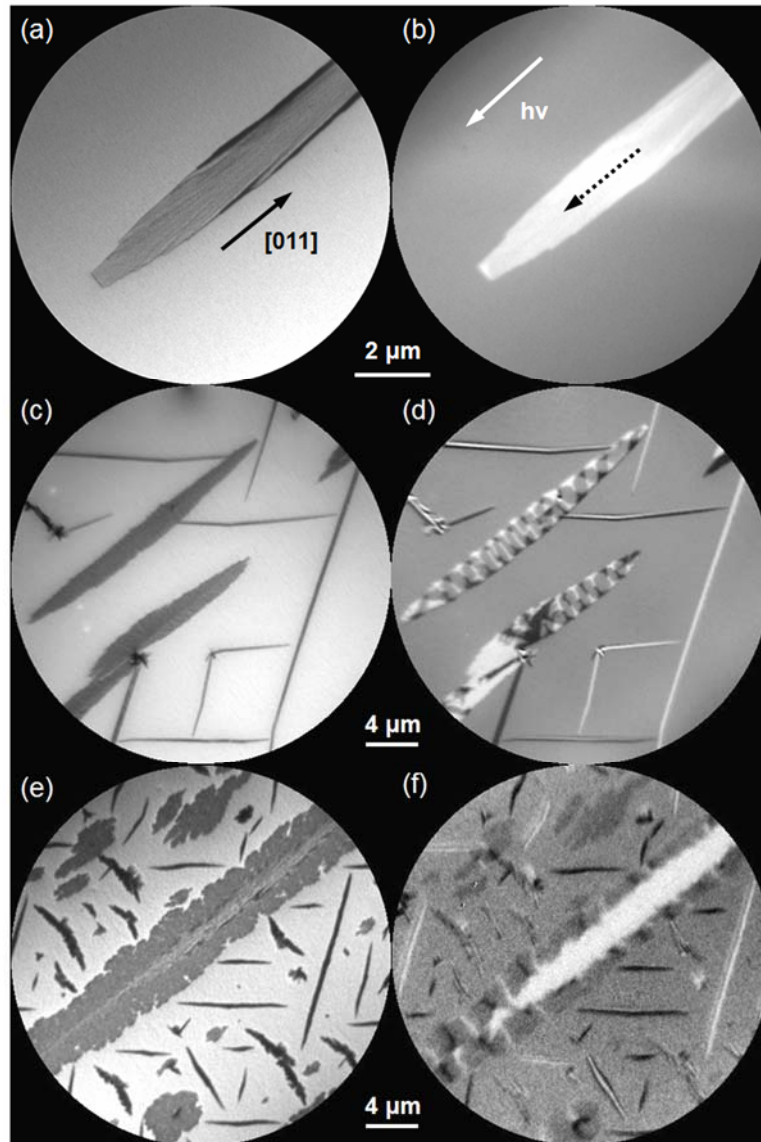


**Figure 9.** (a),(c),(e) LEEM images and (b),(d),(f) corresponding XMCDPEEM images of NWs produced in 3 different growth experiments. (a) LEEM image at 5 eV; (b) Type A NW with single domain structure, the magnetization direction relative to the X-ray incident direction is marked by a dotted arrow; (c) LEEM image at 3 eV; (d) Type A NWs with closure domain structure, type B NWs with single domain structure; (e) LEEM image at 5 eV; (f) Type A NW with single domain (central part) and closure domain structure (dendritic side parts). Photon energy in (b),(d) and (f) 707 eV.

370°C have flat ends (figure 9(a)). The magnetic structure of these simple type-A NWs is predominantly single domain structure, with magnetization along the long direction corresponding to the [011] direction in this example (figure 9(b)).

When Fe was deposited by the variable temperature approach, the shapes of the NWs and their magnetic domain structures are quite different. Figures 9(c) and 9(d) show NWs grown by gradually reducing the temperature from 368°C to 275°C during deposition. Type A NWs have complex shape with sharp tips. These complex A NWs have a magnetic closure domain structure (figure 9(d)). The needle-like type-B NWs, formed under this growth condition, are in single domain state as seen by their homogeneous contrast. Their magnetization component with respect to the direction of the photon beam (indicated in (b)) points in opposite directions, as indicated by the black or white contrast. Figure 9(e) and 9(f) show nanowires grown by a different procedure: after the deposition of 2 ML Fe at 372°C the sample remained at this temperature. The deposition was restarted 40 min later during reduction of the temperature to 260°C. Type A NWs have now dendritic shape. The magnetic structure is a combination of a single domain (central part) and closure domains in the dendritic parts (figure 9(f)). The type B NWs in the same figure 9(f) are thin and long with single domain magnetic structure like in figure 9(d). The differences between the domain structures of the type A wires prepared in different ways can be related to differences in shape, dimension, structural ordering or even a possible change of the chemical composition.

By monitoring the magnetic signal in the XMCDPEEM image at elevated temperatures, we have investigated the Curie temperature of the NWs. Although at temperatures above 400°C the NWs started slowly to decay, the magnetic contrast of all NWs remains strong even after heating at 450°C for 20 min. After heating to 470°C for 20 min the surface decomposed and the NWs disappeared except for some small pieces of type A, which still remained and showed magnetic contrast. The Curie temperature of type A NWs is above

470°C in agreement with the expected Curie temperature of Fe. The Curie temperature of type B NWs likewise exceeds 450°C.

### 3.4. Thermal instability (Decomposition)

Earlier reports described how growth and at higher temperature up to 400°C and post-growth annealing for longer times can produce longer NWs with lower density [2, 3]. In order to explore the possibility of extending these desired trends, we have studied the growth and post growth annealing in LEEM and SPELEEM in situ above 400°C. At elevated temperatures we observed thermal instability (decomposition), which depends strongly upon temperature, heating rate and annealing time. These observations rule out experiments in this elevated temperature range as an approach to produce even longer NWs.

Slow decomposition of the nanowires starts already at about 400°C. Depending on the specific annealing conditions, the type A NWs (Fe crystals) are stable up to 440°C where their length starts to decrease. This is illustrated by the images in figure 10 from an experiment in which the sample was held at 440°C for 20 min. The LEEM image (figure 10(a)) shows that a part of the crystal has disappeared and left a foot print on the substrate

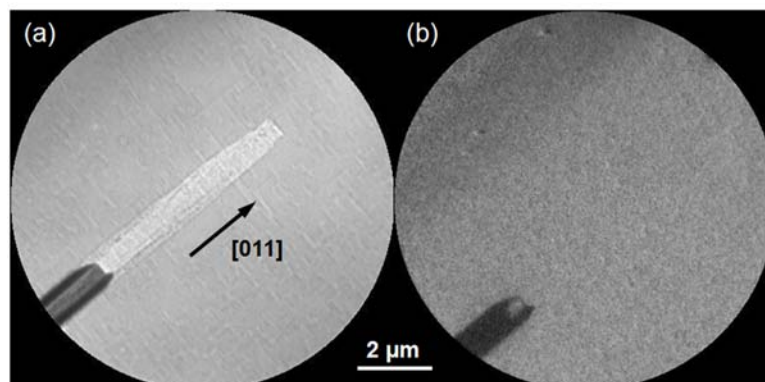


**Figure 10.** Decomposition of type A NW after heating at 440°C for 20 min. (a) The LEEM contrast of the upper part of the NW changed from dark to bright during annealing, LEEM image at 7.2 eV, (b) XMCDPEEM image shows no magnetic contrast of that part of the NW. Photon energy 707 eV.

where it was prior to annealing. The disappearance of the NW is confirmed by the lack of magnetic contrast in this region in the XMCDPEEM image (figure 10(b)). We believe that the Fe of the type A NWs dissolves in the (Fe,Zn)S layer. In a different experiment, the sample was heated at a rate of 3.3°C/min from the growth temperature 360°C up to 450°C for 20 min. Above 420°C the films begin to become heterogeneous. In the Fe 3p XPEEM image after the annealing, the regions surrounding the NWs appear brighter than those further away (Fig. 11a). In the Fe L<sub>3</sub> X-Ray Absorption Spectroscopy (XAS) image (not shown), many small dark features additionally develop in the film, predominantly in the regions further away from the nanowires. In the Zn 3d XPEEM image, on the other hand, the regions further away from the NWs appear brighter than those near to them. Furthermore, the features that appeared dark in the Fe L<sub>3</sub> XAS image now appear bright in the Zn 3d image (Fig. 11b). We attribute the general XPEEM and XAS image brightness changes caused by annealing to diffusion of Fe deeper into the ZnS film and possibly into the underlying GaP substrate. Close to the NWs, the loss of Fe from the (Fe,Zn)S reaction layer due to its deeper segregation is at least partially compensated for by diffusion of Fe from the nanowires which start to dissolve in this temperature region, causing the brightness variations mentioned. The

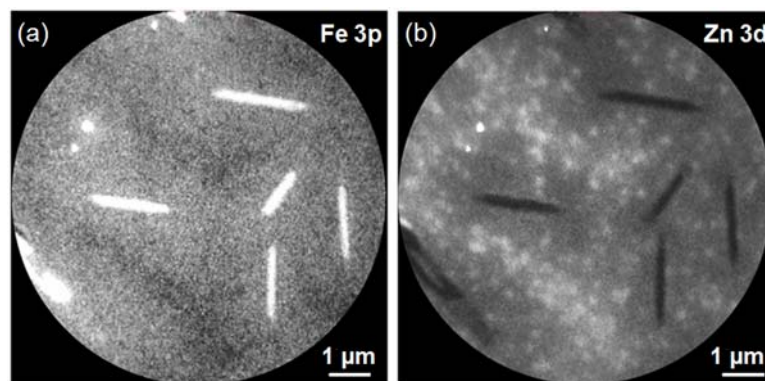


**Figure 11.** Thermal instability after heating up to 450°C for 20 min. (a) XPEEM Fe 3p image shows very fine-grained Fe contrast in the surroundings of both types NWs. One type A NW is in the lower left, the other five NWs are type B; (b) XPEEM Zn 3d image shows a high density of Zn-rich features far away from the NWs. Photon energy 260 eV.

small features that appear dark in the Fe L<sub>3</sub> XAS image are attributed to complete local loss of Fe in the reaction layer, possibly at unidentified defects, e.g. threading dislocations. In the absence of external Fe supply from an incident Fe flux during these annealing experiments, no replacement of Zn by Fe occurs as it does during deposition and therefore no further Zn desorption occurs. The small features grow in number and size with increasing temperature. The type B NWs composed of greigite start to recede at 450°C. The remaining parts of the NWs are still magnetic. Figure 11 shows one NW type A in the lower left and five NWs type B after annealing at 450°C for 20 min. The brighter regions surrounding the NWs are also present in the Fe L<sub>3</sub> XAS image but absent in the XMCDPEEM image and we conclude therefore that the Fe in these regions is nonmagnetic, presumably in the form of FeZnS. After heating to 470°C for 20 min all NWs have disappeared, except for small parts of the larger type A NWs. The layer is now very heterogeneous and XPEEM shows Zn and Fe everywhere with locally varying concentration related to the original crystal location. In addition Ga from the GaP below the ZnS epitaxial layer has diffused to the surface or near to it to produce a strong XPS signal. No break-up of the layer is seen within the resolution limit of LEEM.

The changes that happened during the annealing at high temperatures were irreversible. Deposition of Fe on the transformed surface cannot return it to the well-ordered (1x1) structure. Finally, we note that the stability of type B NWs contrasts with the thermal decomposition of natural greigite mineral material above about 280°C that was noted much earlier [42] and more recently of hydrothermally synthesized greigite above 405°C [43]. We speculate that greater thermal stability may be an indication of improved purity of the material. The greigite type B NWs produced in the clean ultrahigh vacuum environment here may be further stabilized against the loss of S by the ZnS substrate that can serve as a S reservoir. This allows the determination of a new lower bound on the Curie temperature, 450°C, of greigite in our work that is higher than previously reported [43].

#### 4. Summary

The growth of Fe on ZnS(100) at temperatures above 360°C produces a FeZnS reaction layer before three-dimensional crystals nucleate. A large variety of crystals form, whose number and shape depends strongly upon temperature and growth conditions.

We have studied the growth, structure, composition and magnetic properties of elongated crystals (nanowires) called type A and type B using a variety of surface characterization techniques, including LEEM,  $\mu$ LEED, PEEM,  $\mu$ XPS and XMCDPEEM. According to the XPS data discussed above, type A nanowires consist of pure Fe covered with S adsorption layer. The XMCDPEEM images demonstrate that type A nanowires are ferromagnetic in the single domain state except wider, dendritic type A nanowires, which show complex closure domain patterns. The magnetization direction is along the [011] direction, which is not the easy magnetization direction of the bcc-Fe but very likely due to shape anisotropy. Based on these results and on the LEED measurements, we concluded that the type A nanowires are bcc-Fe crystals with parallel orientation with respect to the substrate, elongated along the Fe[011] direction. This conclusion is also in agreement with the earlier finding based upon selected area electron diffraction (SAED) pattern [2-4].

The identification of the type B nanowires as greigite ( $\text{Fe}_3\text{S}_4$ ) is based on the XPS measurements, which suggested a Fe-S compound, on the compatibility of the greigite structure with the measured LEED pattern and also on its magnetism at least up to 450°C. This result is different from the earlier conclusion that type-B nanowires are bcc-Fe [2-4]. This could be due to the different experimental conditions, e.g. the different Fe deposition rates.

For the growth of the type B nanowires the formation of FeZnS reaction layer at high temperatures is necessary. The longest needle-like type B nanowires (with length to width

ratio up to 500:1) were grown using the variable temperature approach starting at high temperatures followed by cooling down.

All nanowires have facets and are unstable upon heating at 450°C for 20 min due to the ZnS substrate decomposition. The magnetic contrast of type A NWs persists until they almost completely disappeared after heating to 470°C for 20 min. The magnetic contrast of type B NWs was still observed after heating to 450°C for 20 min.

### **Acknowledgment**

Financial support from the Hong Kong Research Grant Council under grant HKUST 603808 is gratefully acknowledged.

### **References**

- [1] Wastlbauer G and Bland J A C 2005 *Adv. Phys.* **54** 137
- [2] Lok S K, Chan S K, Wong G K L and Sou I K 2009 *J. Cryst. Growth* **311** 2208
- [3] Sou I K, Lok S K, Wang G, Wang N and Wong G K L 2010 *J. Electron. Mater.* **39** 882
- [4] Lok S K, Tian J C, Wang Y, Lai Y H, Lortz R, Petrovic A, Panagopoulos C, Wong G K L, Wang G, and Sou I K 2012 *Nanotechnology* **23** 485605
- [5] Almawlawi D, Coombs N and Moskovits M 1991 *J. Appl. Phys.* **70** 4421
- [6] Whitney T M, Searson P C, Jiang J S and Chien C L 1993 *Science* **261** 1316
- [7] Hultgren A, Tanase M, Chen C S, Meyer G J and Reich D H 2003 *J. Appl. Phys.* **93** 7554
- [8] Barbic M and Scherer A 2005 *Nano Lett.* **5** 187
- [9] Chan E T, Kan J J, Doran C, Ouyang L, Smith D J and Fullerton E E 2010 *Nano Lett.* **10** 5070

- [10] Allwood D A, Xiong G, Faulkner C C, Atkinson D, Petit D and Cowburn R P 2005 *Science* **309** 1688
- [11] Parkin S S P, Hayashi M and Thomas L 2008 *Science* **320** 190
- [12] Koyama T *et al* 2011 *Nat. Mater.* **10** 194
- [13] Velev J, Sabirianov R F, Jaswal S S and Tsymbal E Y 2005 *Phys. Rev. Lett.* **94** 127203
- [14] Bauer E 1994 *Rep. Prog. Phys.* **57** 895
- [15] Altman M S 2010 *J. Phys.: Condens. Matter* **22** 084017
- [16] Locatelli A, Aballe L, Menteş T O, Kiskinova M and Bauer E 2006 *Surf. Interface Anal.* **38** 1554
- [17] Locatelli A and Bauer E 2008 *J. Phys: Condens. Matter* **20** 093002
- [18] Lefèvre C T, Menguy N, Abreu F, Lins U, Pósfai M, Prozorov T, Pignol D, Frankel R B and Bazylinski D A 2011 *Science* **334** 1720
- [19] Qian X F, Zhang X M, Wang C, Xie Y, Wang W Z and Qian Y T 1999 *Mater. Sci. Eng. B* **64** 170
- [20] Cao F, Hu W, Zhou L, Shi W, Song S, Lei Y, Wang S and Zhang H 2009 *Dalton Trans* 9246
- [21] Zhang Z J and Chen X Y 2009 *J. Alloy Compd.* **488** 339
- [22] Vanitha P V and O'Brien P 2008 *J. Am. Chem. Soc.* **130** 17256
- [23] Zhang Y, Du Y, Xu H and Wang Q 2010 *Cryst. Eng. Comm.* **12** 3658
- [24] Beal J H L, Prabakar S, Gaston N, Teh G B, Etchegoin P G, Williams G and Tilley R D 2011 *Chem. Mater.* **23** 2514
- [25] Paolella A *et al* 2011 *Chem. Mater.* **23** 3762
- [26] Chang Y S, Savitha S, Sadhasivam S, Hsu C K and Lin F H 2011 *J. Colloid Interface Sci.* **363** 314

- [27] Feng M, Lu Y, Zhang M, Xu Y J, Gao H L, Dong L, Xu W P and Yu S H 2013 *Scientific Reports* **3** 2994
- [28] Akhtar M, Malik M A, Tuna F and O'Brien P 2013 *J. Mater. Chem. A* **1** 8766
- [29] Pankhurst Q A, Connolly J, Jones S K and Dobson J 2003 *J. Phys. D: Appl. Phys.* **36** R167
- [30] Gao M R, Xu Y F, Jiang J and Yu S H 2013 *Chem. Soc. Rev.* **42** 2986
- [31] Legg K O, Jona F, Jepsen D W and Marcus P M 1977 *Surf. Sci.* **66** 25
- [32] Benziger J B and Madix R J 1980 *J. Electron Spectrosc. Relat. Phenom.* **20** 281
- [33] Chen Z H, Sokolowski M, Stadler F, Schneider M, Fink R and Umbach E 2002 *Europhys. Lett.* **59** 552
- [34] Weiss W, Schmeisser D and Göpel W 1989 *Surf. Sci.* **207** 401
- [35] Yasue T, Koshikawa T, Jalochoowski M and Bauer E 2001 *Surf. Sci.* **493** 381
- [36] Tang W X, Man K L and Altman M S 2002 *J. Vac. Sci. Tech. B* **20** 2492
- [37] Klein C *et al* 2011 *Rev. Sci. Instrum.* **82** 035111
- [38] Rickard D and Luther III G W 2007 *Chem. Rev.* **107** 514
- [39] Li Y, van Santen R A and Weber T 2008 *J. Solid State Chem.* **181** 3151
- [40] Bauer E, Man K L, Pavlovska A, Locatelli A, Mentş T O, Niño M A and Altman M S 2014 *J. Matl. Chem. A* **2** 1903
- [41] Lepetit P, Bente K, Doering T and Luckhaus S 2003 *Phys. Chem. Minerals* **30** 185
- [42] Skinner BJ, Erd RC and Grimaldi FS 1964 *The American Mineralogist* **49** 543
- [43] Wang J, Cao S-H, Wu W and Zhao G-M 2011 *Phys. Scr.* **83** 045702